Fire and Materials

WILEY

RESEARCH ARTICLE OPEN ACCESS

Altitude Effects on Ejected Flames in Façade Calibration Tests: Experimental and Numerical Investigation

Xukun Sun[1,2,3] | Hideki Yoshioka[3] | Takafumi Noguchi[3] | Yuhei Nishio[4] | Biao Zhou[5]

[1]School of Safety Engineering, Beijing Institute of Petrochemical Technology, Beijing, China | [2]Beijing Academy of Safety Engineering and Technology, Beijing, China | [3]Department of Architecture, Faculty of Engineering, The University of Tokyo, Tokyo, Japan | [4]Department of Fire Engineering, Building Research Institute, Ibaraki, Tsukuba, Japan | [5]School of Emergency Management and Safety Engineering, China University of Mining & Technology (Beijing), Beijing, China

Correspondence: Hideki Yoshioka (yoshioka@arch1.t.u-tokyo.ac.jp)

Received: 29 April 2025 | **Revised:** 29 April 2025 | **Accepted:** 21 August 2025

Funding: This work was supported by Japan Society for the Promotion of Science (22KK0062).

Keywords: altitude effect | calibration test | CFD modeling | façade fire | large scale

ABSTRACT

Ejected flames from a compartment opening pose a significant fire hazard to building fire safety, serving as a trigger of rapid façade flame spread. Although extensively studied under standard altitude conditions, their fire behavior under subatmospheric pressure remains to be further explored. This study investigates the altitude effect on ejected flames through a combination of large-scale experiments and Computational Fluid Dynamics (CFD) modeling. JIS A 1310 calibration tests were conducted at HRRs (Heat Release Rates) ranging from 600 to 900 kW, revealing that the flame turning point is minimally affected by input HRR for apparent flame ejection. Subsequently, CFD modeling is validated by utilizing measured temperatures across horizontal distances of 0–0.8 m from the façade centerline and vertical heights of 0–2.6 m above the upper edge of the opening. Extending the validated modeling conditions, the altitude effect on façade flames under varied HRRs and opening factors is clarified. Results indicate that subatmospheric pressures contribute to the expansion of flame temperature distributions with lower inner flame temperatures, attributed to reduced oxygen entrainment mass flow rates caused by decreased air density. Among the opening configurations, horizontal openings pose a higher fire hazard. An improved Yokoi-Lee model introducing the HRR factor Q'_p is developed to account for fuel combustion outside the chamber induced by variations in input HRR, opening factors, and atmospheric pressure.

1 | Introduction

In recent years, advancements in construction technology and rapid urbanization have led to a significant increase in both the height and volume of modern buildings [1]. Consequently, the occurrence of building fires, particularly façade fires, has become a critical concern due to the potential for rapid flame spread, posing severe threats to life safety and property [2]. Façade fires are typically initiated by window-ejected flames from compartment fires, which ignite exterior cladding materials, enabling sustained combustion. This process contributes to vertical fire propagation along the building's exterior and facilitates the leapfrog effect, enabling fire to spread across multiple floors.

To characterize façade flames, the pioneering work by Yokoi [3] introduced the concept of non-dimensional temperature Θ. Building on this, Lee and Delichatsios et al. [4] defined the length scales for window-ejected flame, whereas Ohmiya et al. [5] and Zhou et al. [6] refined Yokoi's model by incorporating a virtual heat source and a variable neutral plane to improve the model convergence. However, existing studies primarily focus on façade flames at standard altitudes, despite the fact that there are still large cities with façade fire risk situated at altitudes as high as 4000 m [7], as shown in Figure 1. At these elevations, reduced atmospheric pressure and lower effective oxygen concentrations significantly impact combustion and fuel burning rates [10–13], thereby altering fire dynamics and temperature profiles [14].

Regarding the effects of altitude on fire behavior, available research has explored both experimental and numerical aspects. Experimental studies on pool fires under subatmospheric pressure revealed that flame behavior transitions from turbulent to laminar, with the flame turning blue as pressure decreases [14]. Under the scenario of fire at varied façade angles, Ma et al. [10, 12] analyzed the combustion of polyurethane foam at low ambient pressure, showing that combustion is limited under reduced pressure, larger inclination angles, and wider specimens, while reduced pressure contributes to increased flame height [11]. On the numerical side, altitude effects on tunnel fires have been studied by modifying theoretical correlations to predict smoke back-layering length [15] and tunnel temperature distribution [16] under reduced pressure. Within this scope, research on window-ejected flames in façade fire tests at varying altitudes remains limited, and the validation of corresponding numerical modeling on large scales is also deficient.

This study combines large-scale calibration tests of flame ejection with Computational Fluid Dynamics (CFD) modeling to explore the altitude effect on façade fire behavior. The experiments elucidate the impact of HRRs (Heat Release Rates) on flame intensity and provide a basis for validating the CFD modeling. Building on this foundation, the altitude effect on ejected flames is investigated by varying HRRs, opening factors, and atmospheric pressures. Furthermore, by characterizing the HRR outside the chamber, the flame temperature is non-dimensionally correlated and converged using an improved model, offering a comprehensive approach to understanding façade flame behavior under varying altitude conditions.

2 | Experimental and Numerical Configurations

2.1 | Facilities and Measurement Setup

A series of experiments is conducted with a large-scale platform, which is established based on JIS A 1310 [17], as shown in Figure 2. The platform primarily consists of a chamber and a façade, connected by a square opening that serves as the passage for fire. The chamber was constructed with a 50 mm-thick inner layer of alumina fiber blanket and a 150 mm-thick outer layer of ceramic fiber block. A burner, located at the rear of the chamber, was supplied with propane of 98.7% purity to generate the designated HRRs. To maintain a steady gas flow rate, the burner was filled with ceramic fiber balls. With respect to the façade, the combustible materials are not involved, that is calibration test, which is constructed by two layers of 12 mm thick calcium silicate board, with the surface covered by a 25 mm-thick ceramic fiber blanket. Since the focus of this setup is the behavior of ejected flames, flame temperatures were measured using a stainless steel net equipped with 136 thermocouples. The thermocouple net was positioned along the centerline, perpendicular to the façade surface. In this case, sheathed-type thermocouples were installed near the opening, whereas glass-coated thermocouples were placed in the outer region, with diameters of 3.2 and 0.65 mm, respectively. The sheathed-type thermocouples can withstand temperatures ranging from 950°C to 1050°C, whereas the glass-coated type is capable of measuring temperatures around 600°C, with uncertainties of ±0.75% and ±2.5°C, respectively. The target HRRs were set to 600, 750, and 900 kW by adjusting the propane flow rates to 433, 541, and 649 L/min (at 20°C and 1 atm), respectively, representing weak, intermediate, and strong flame ejections [18]. The experimental duration for each HRR was 5 min, generally achieving a quasi-steady state in the final 3 min, which was used to obtain the time-averaged temperature. All the experiments were conducted at the Building Research Institute (BRI) of Japan in Tsukuba, considered standard pressure and altitude [19]. The detailed experimental conditions can be found in Table 1.

2.2 | Numerical Modeling

In this study, the CFD tool of FireFOAM [20] was employed, which is an OpenFOAM solver developed by FM Global for

FIGURE 1 | Cities of (a) La Paz [8], Bolivia, located at 3640 m above sea level, and (b) Dali [9], China, located at 2000 m above sea level.

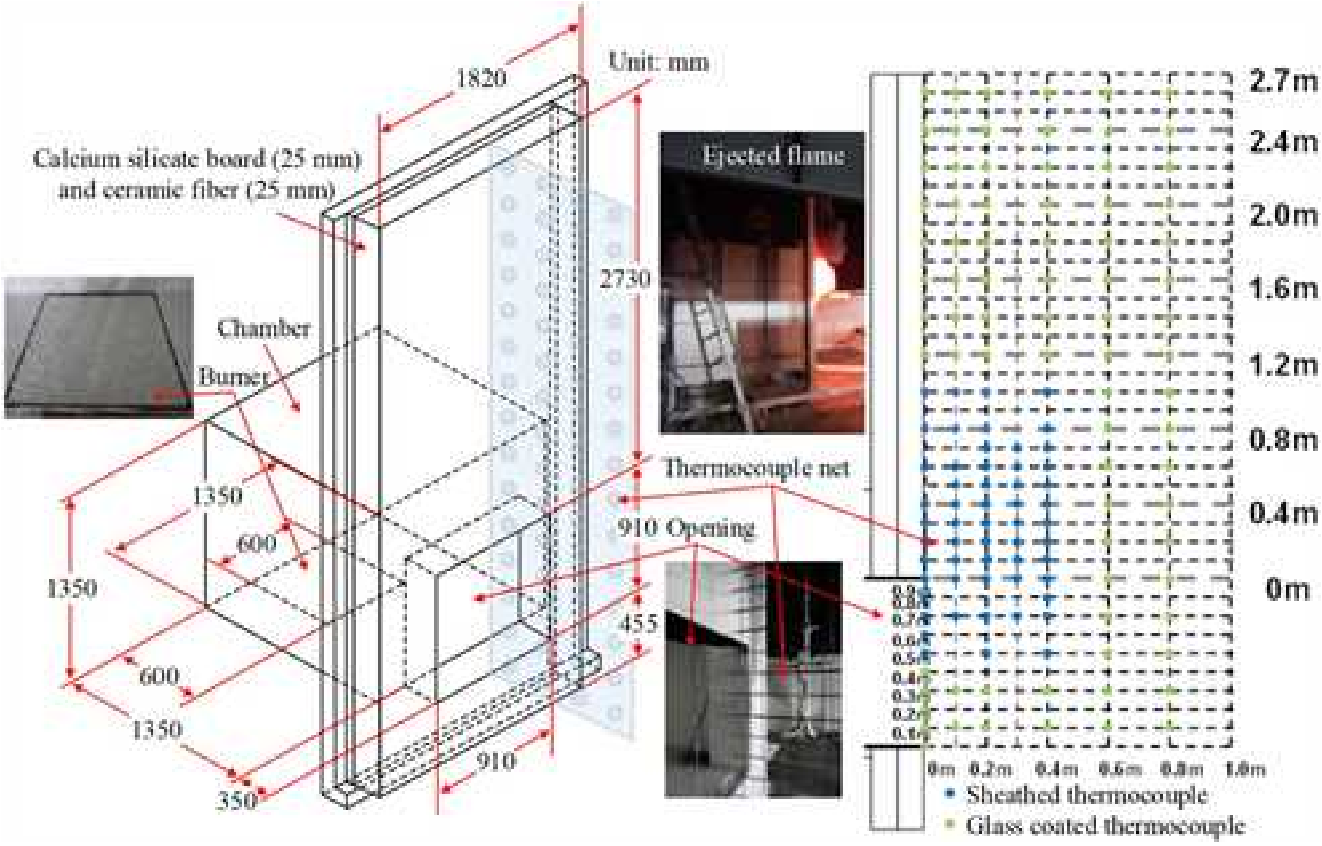

FIGURE 2 | Dimensions and layout of facilities.

TABLE 1 | Summary of experimental conditions.

Opening dimension (m)	Target HRR (kW)	Volumetric flow rate (L/min)	Altitude (m)	Atmospheric pressure (kPa)	Effective oxygen percentage (%)
$W \times H = 0.91 \times 0.91$	600	433	0	101.3	20.9
	750	541			
	900	649			

the numerical modeling of fire spread and suppression. In the case of buoyancy-driven flow and diffusion combustion [21, 22], the performance of FireFOAM has been verified with acceptable accuracy in both temperature and radiation prediction.

In FireFOAM, large eddy simulation (LES) is employed using the finite volume method (FVM), where turbulence is resolved for mesh sizes larger than the filter width $\triangle = \sqrt[3]{\triangle x \triangle y \triangle z}$ [23]. For the eddies smaller than this filter, that is sub-grid scale (SGS), it is addressed by the turbulence model. In this study, the one-equation eddy viscosity SGS model [24] was utilized, with input coefficients of $C_k = 0.03$ and $C_\epsilon = 1.048$. Turbulence combustion was considered using the modified eddy dissipation concept (EDC) model [25], with parameters of $C_{EDC} = C_{Diff} = 1$, which provided good estimation of fuel reaction rate during the transition from laminar to turbulent flow, as well as for fully developed turbulent flames [21]. For radiation modeling, the discrete ordinate method was employed, which considers high-temperature gases using the gray mean absorption-emission approach [26]. The radiative transfer equation (RTE) was solved with 48 solid angles, and the radiative heat loss was accounted for using a constant radiant fraction of 0.2. Further modeling details can be found in Ref. [18].

With the objective of getting the accurate facade temperature, the thermocouple model was employed to calculate the thermal balance for the thermocouple bead, which was introduced by LES-based estimates of the radiative and convective heat transfer [26]. The model is expressed as:

$$\rho_{TC} C_{p,TC} V_{TC} \frac{dT_{TC}}{dt} = \varepsilon_{TC}\left(G - \sigma T_{TC}^4\right) A_{TC} + h\left(T_g - T_{TC}\right) A_{TC}$$

where ρ_{TC}, $C_{p,TC}$, V_{TC}, A_{TC} and ε_{TC} denote the density, heat capacity, volume, surface, and emissivity of the thermocouple bead. T_{TC} is the thermocouple bead temperature, T_g is the simulated gas temperature, and the heat transfer coefficient h is obtained from the Nusselt number.

In alignment with the experimental setup, the computational domain was generated to include both the chamber and façade regions, as illustrated in Figure 3. To allow for sufficient air entrainment, the façade region was defined with dimensions of $W \times L \times H = 4\,\text{m} \times 4\,\text{m} \times 5\,\text{m}$, with the surroundings treated as open boundaries. For the mesh configuration, a baseline mesh size of 10 cm was used, while regions with turbulent flames, such as the chamber and areas near the façade, were refined to a mesh size of 2.5 cm to capture the flame dynamics accurately. The 1-D heat transfer within the façade was considered by extruding a solid region perpendicular to the façade surface, with a thickness of 5 cm. Here, the mesh along the surface-normal direction was refined into 150 layers. Since the ceramic fiber blanket and calcium silicate board used in the experiment are non-combustible, pyrolysis was not considered in the model, with material properties referenced from Ref. [18]. In this case, HRR is determined by summing the chemical heat of each grid. By characterizing the grid regions, the HRR inside and outside the chamber is extracted to clarify the behavior of ejected flames.

In contrast to the square opening and standard altitude used in the experiments, the numerical modeling includes extended conditions with varied opening shapes (the validation cases, compared to the experiments, adjust the opening dimensions from $W \times H = 0.91\,\text{m} \times 0.91\,\text{m}$ to $W \times H = 0.9\,\text{m} \times 0.9\,\text{m}$ to accommodate mesh generation) and atmospheric pressures. For the opening shapes, the ventilation capacity is characterized by the opening factor $A\sqrt{H}$, where A is the opening area in m^2 and H is the opening height in m. Altitudes ranging from 0 to 4450 m are considered, with the corresponding atmospheric pressures adjusted between 58.11 and 101.325 kPa, resulting in effective oxygen percentages of 11.9%–20.9% [19]. Detailed modeling conditions are provided in Table 2. Here, the opening shape is defined as vertical when the opening ratio $n > 1$ and horizontal when $n < 1$, thereby providing two respective conditions for vertical and horizontal openings. In this case, opening ratios of 0.5–2 are considered, representing common scenarios in façade fire spread [27, 28].

3 | Result and Discussion

3.1 | Experimental Description of Façade Flames

The experimentally measured temperature distributions and flame morphologies along the façade are shown in Figure 4. On the left side of Figure 4, vertical temperature distributions at varying horizontal distances (0–0.8 m) from the façade surface

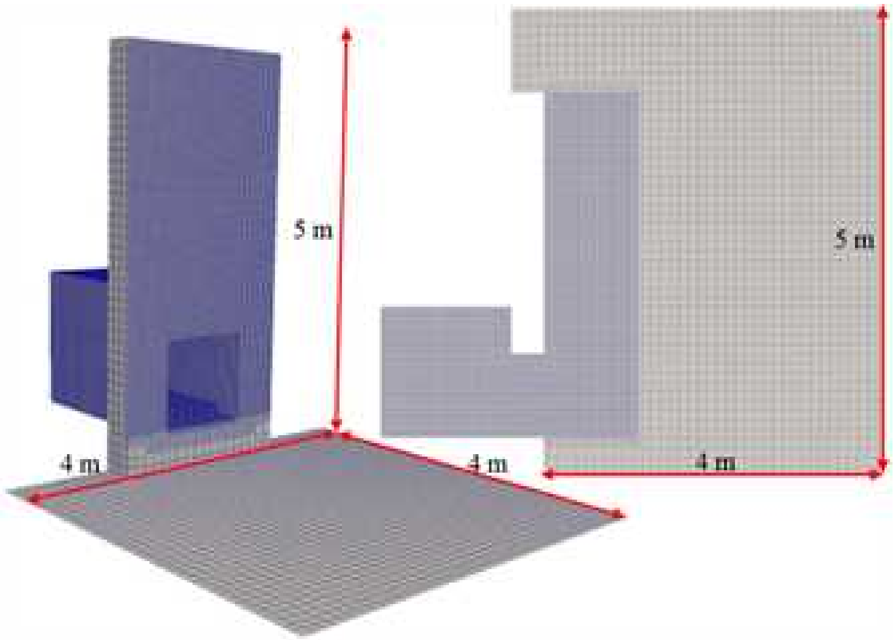

FIGURE 3 | The computational domain and mesh slice.

TABLE 2 | Modeling conditions.

Opening dimension		Opening ratio	$A\sqrt{H}$	Target		Atmospheric	Effective oxygen
W (m)	**H (m)**	**($n = H/W$)**	**($\text{m}^{5/2}$)**	**HRR (kW)**	**Altitude (m)**	**pressure (kPa)**	**percentage (%)**
0.9	0.9	1	0.768	600, 750, 900	0, 784, 1698, 2692, 3840, 4450	101.3, 92.3, 82.5, 72.9, 62.9, 58.1	20.9, 18.9, 16.9, 14.9, 12.9, 11.9
0.7	0.9	1.29	0.598				
0.9	0.675	0.75	0.499				
0.45	0.9	2	0.384				
0.9	0.45	0.5	0.272				

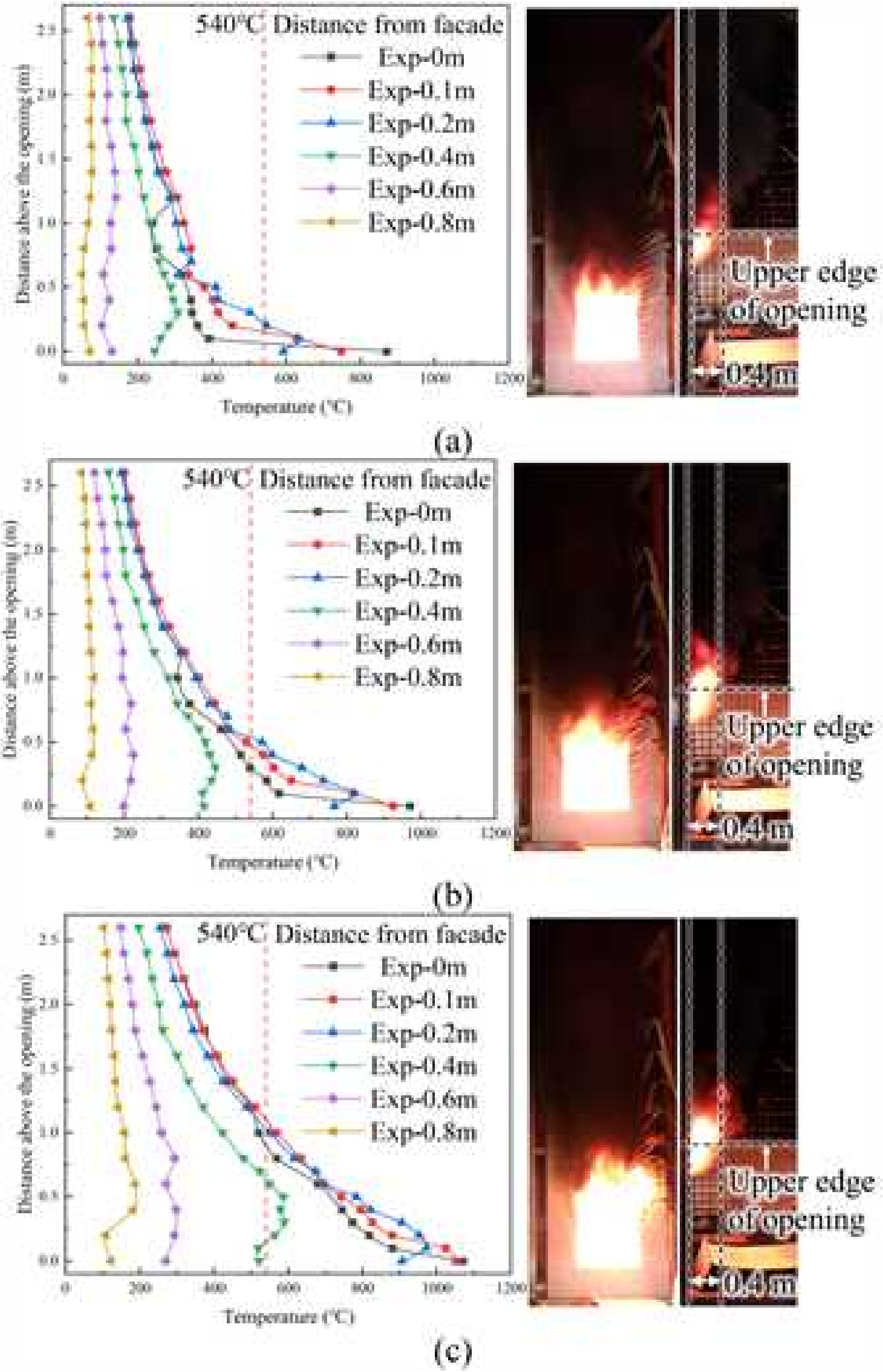

FIGURE 4 | Vertical temperature distribution with increasing horizontal distance from the façade surface, and ejected flames at HRRs of (a) 600 kW, (b) 750 kW, and (c) 900 kW.

are measured by the thermocouple net. With the flame tip temperature defined as 540°C [29], flame thickness and height under HRRs of 600–900 kW were obtained based on the vertical and horizontal temperature distributions. For HRRs of 600 and 750 kW, flame thicknesses remain below 0.4 m, whereas at 900 kW, enhanced combustion near the opening increases flame thickness to 0.4–0.6 m. Flame height, more affected by HRR than flame thickness, is measured as 0.25, 0.5, and 1.25 m for HRRs of 600, 750, and 900 kW, respectively. Note that the temperature peaks at horizontal distances of 0.2 and 0.4 m are persistent at different HRRs, indicating flame turning positions—representing the transition point where flame behavior shifts from horizontal momentum-dominated to buoyancy-dominated, that is the inflection point of ejected flames—occur within 0.1–0.2 m from the façade surface. Additionally, the positions of temperature peaks consistently appear at the heights of 0.1 and 0.4 m for horizontal distances of 0.2 and 0.4 m, respectively, indicating that for apparent façade flames, the ejected flame temperature near the opening is primarily determined by the HRR inside the chamber. In this case, for a given chamber geometry, the flame turning point is minimally influenced by variations in input HRRs.

On the right side of Figure 4, the front and side views of the ejected flame are presented. Aligning with the flame behaviors determined by 540°C in temperature distributions, the façade flames become more intense according to the enlarged luminous regions for HRRs of 750 kW and above, with a fire plume appearing at heights above 0.25 m at 600 kW. However, the observable increase in flame intensity between 750 and 900 kW is marginal, limited to a visible flame height of approximately 0.5 m. This is attributed to significant soot production at 900 kW, which increasingly obscures the flame morphology.

3.2 | Validation of Numerical Modeling

Before proceeding with the extended analysis based on numerical modeling, it is essential to confirm the reliability of the model. Given that LES is employed in this study, accurately capturing turbulent flames is dependent on mesh size; thus, the results of the numerical modeling must be mesh independent. To verify this, a mesh sensitivity analysis was performed in the region with intense turbulent flames, that is the opening region of $W \times H = 0.9\,\mathrm{m} \times 0.9\,\mathrm{m}$ at 900 kW HRR and standard altitude, using various mesh sizes, as shown in Figure 5. Four mesh sizes, ranging from 1.25 to 10 cm, are evaluated, with outflow temperature and velocity used for comparison. It can be found that both temperature and velocity converge at finer mesh sizes, while coarser meshes tend to overestimate the region of outflow flames. With mesh refinement, the neutral plane [6] elevates, reaching an approximate height of 0.5 m. Generally, results with mesh sizes of 2.5 and 1.25 cm are closely aligned, with the 1.25 cm mesh providing more detailed fluctuations in the turbulent flames. Considering the balance between computational cost and accuracy, the 2.5 cm mesh size is deemed a cost-effective resolution that ensures mesh independence in the modeling results.

The experiments in this study are used to validate the modeling conditions with an opening dimension of $W \times H = 0.9\,\mathrm{m} \times 0.9\,\mathrm{m}$ at the standard altitude (0 m elevation). Figure 6 compares the experimental and modeled temperatures at varied horizontal distances and HRRs. Overall, the numerical model achieves qualitative agreement, effectively capturing temperature peaks, particularly for HRRs of 600 and 750 kW. For the 900 kW HRR, at horizontal distances of 0.1 and 0.2 m (within the region of ejected flames), the model underestimates temperatures below 0.5 m height but overestimates them above this height. Notably, this height aligns with the visible flame height shown in Figure 4, suggesting these discrepancies are related to soot production. It is acknowledged that soot contributes to the radiative heat loss in flames [30]; in this case, limited soot generation near the opening results in relatively lower heat loss below 0.5 m, while higher heat loss occurs at higher positions. Since the radiative heat loss in modeling is considered by a constant radiant fraction, the soot impact on heat loss could be over- or under-estimated below and above 0.5 m, respectively, leading to temperature discrepancies. For a horizontal distance of 0.4 m, temperature underestimations consistently appear below 0.5 m across all HRRs. This region is located at the transition boundary between the flame and air entrainment zone, with two possible explanations: (1) current mesh resolution is incapable of capturing the flame boundary accurately, leading to the entrainment of larger amounts of cooler air and thus lower temperatures [22]; (2) uncertainties in the thermocouple model, including the thermophysical properties of the thermocouple bead and the determination of the heat transfer coefficient, contribute to deviations compared to actual thermocouple working conditions.

Aiming for a quantitative evaluation of modeling accuracy, the deviation rate is provided, calculated as the ratio of the difference between modeled and measured temperatures to the measured temperature (averaged across heights for each horizontal distance). In general, the modeled temperature shows good accuracy near the flame trajectory, where the flame remains detached from the façade at 600 kW but reattaches at 750 and 900 kW HRRs, as shown in Figure 4. However, as the distance from the flame increases, the deviation rate increases, which can be attributed to the growing influence of flame radiation compared to heat convection. This phenomenon is not fully captured by the thermocouple model. In this case, the temperature is relatively lower, with indistinct deviations in qualitative comparisons (Table 3).

3.3 | Influence of Altitude Effect on Façade Flames

Using the validated numerical model, the impact of altitude on façade flames was investigated, considering variables of input

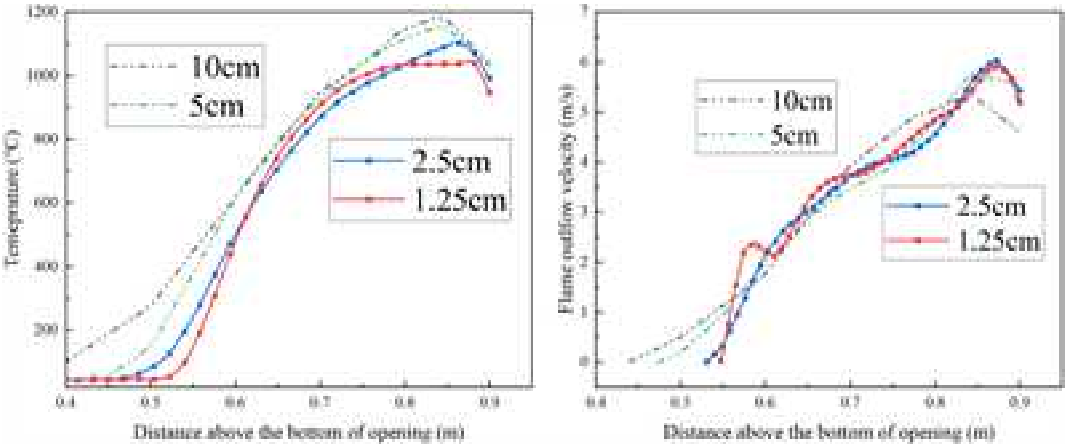

FIGURE 5 | Temperature and velocity of outflow flames varying mesh sizes.

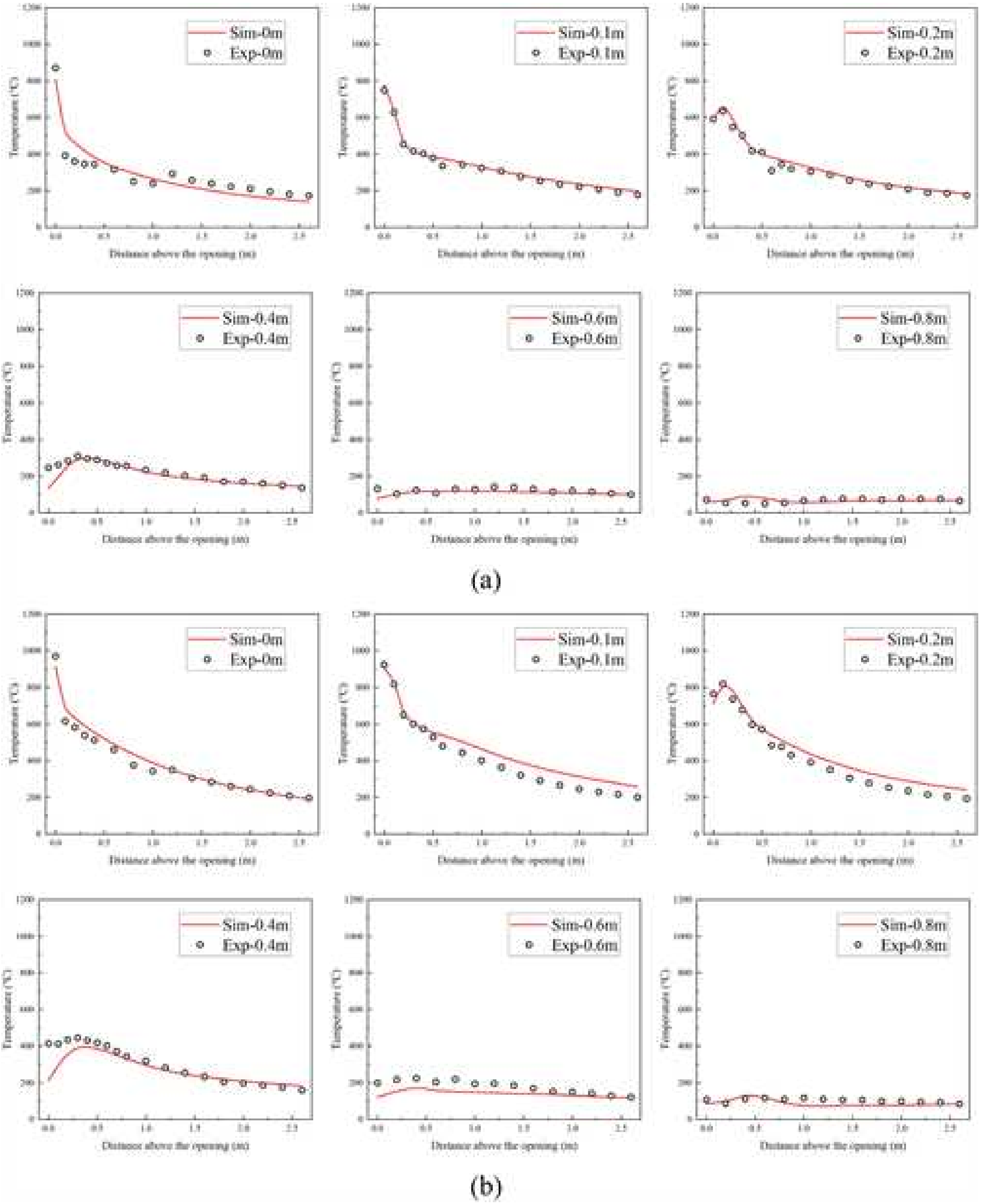

FIGURE 6 | Modeling comparison of vertical temperature distribution varying horizontal distance at different HRRs, (a) 600 kW, (b) 750 kW, and (c) 900 kW.

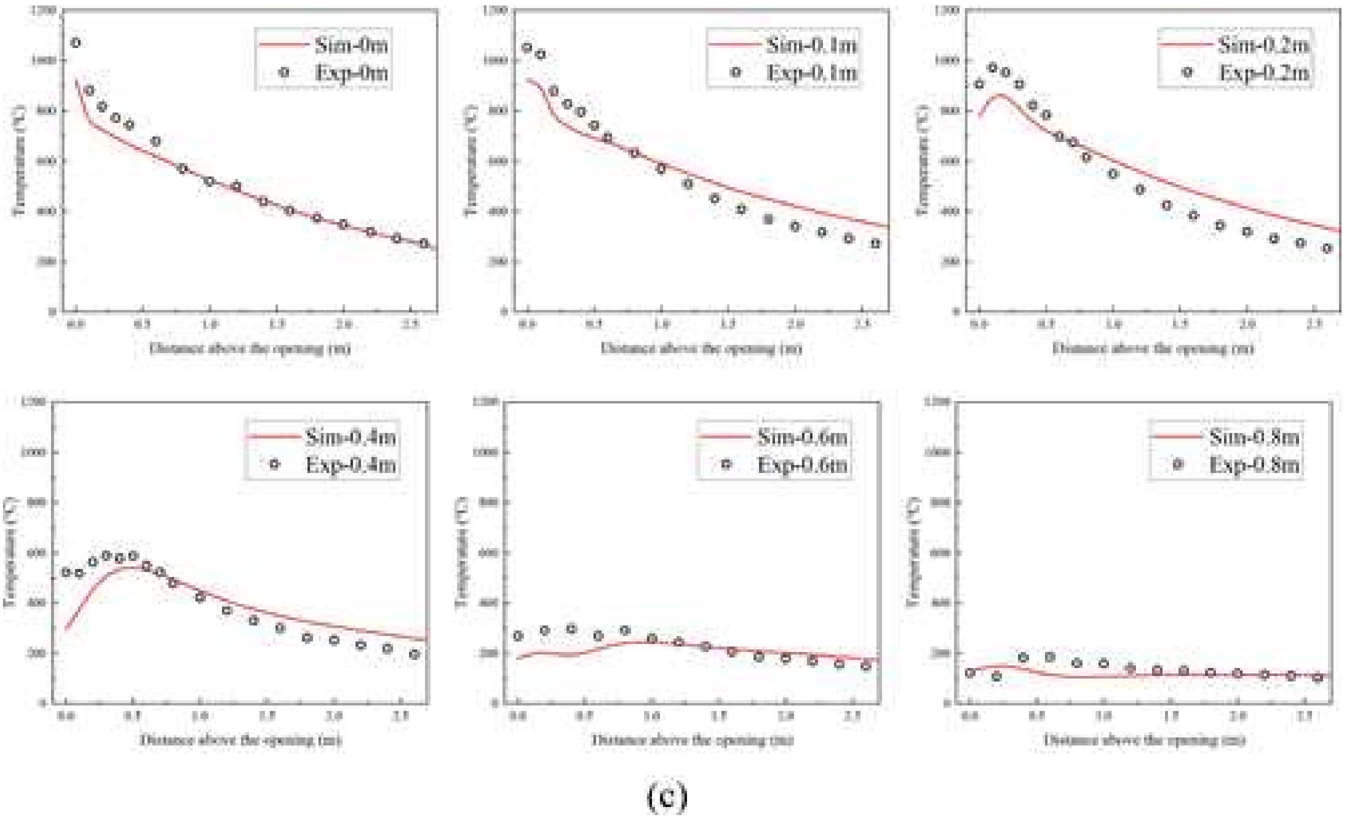

FIGURE 6 | (Continued)

TABLE 3 | Deviation rate of modeling.

HRR (kW)	Horizontal distance from the façade (m)						Average (%)
	0 (%)	0.1 (%)	0.2 (%)	0.4 (%)	0.6 (%)	0.8 (%)	
600	17.7	4.2	5.6	10.2	13.4	18.6	11.6
750	5.3	12.2	11.1	14.7	27.2	25.1	15.9
900	5.4	12.4	14.1	17.9	19.5	22.4	15.3

HRR, atmospheric pressure, and opening factors. Modeling results are presented using the pressure for each altitude, with details provided in Table 1. Essentially, the intensity of façade flames is governed by the amount of fuel combusted inside and outside the chamber, that is HRR inside and outside the chamber. Figure 7 gives the chamber HRR (HRR inside the chamber) with varied opening factors, input HRRs, and pressures. For a certain pressure, chamber HRR depends on the opening factor, reflecting the ventilation capacity of each dimension, regardless of input HRR. A reduced opening factor restricts air inflow, leading to a lower chamber HRR. Additionally, chamber HRR decreases with lower pressure, due to reduced oxygen content and mass flow rate limiting complete fuel combustion [14]. It is worth noting that the sensitivity of chamber HRR to varying pressures is changed by opening shapes. Figure 7 shows the slopes of the linear fitted lines, which indicates that square and vertical openings exhibit similar reductions in chamber HRR with decreasing pressure. However, horizontal openings with an opening factor of 0.499 are more sensitive to pressure variations; the reason is that this opening provides a relatively larger interaction surface between

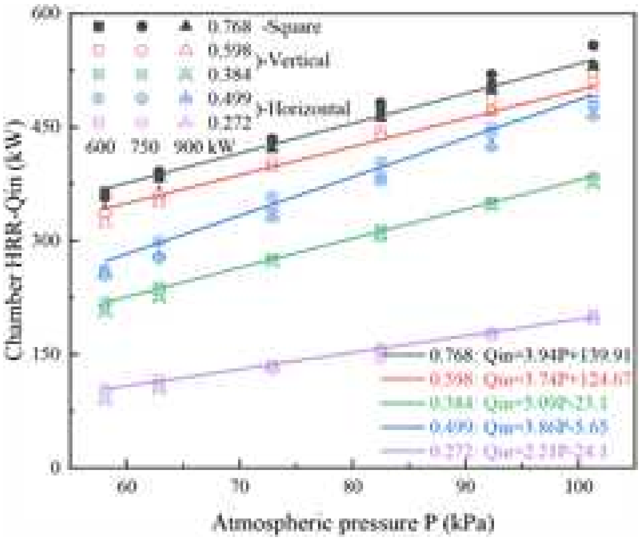

FIGURE 7 | Chamber HRRs varying input HRRs, opening factors, and pressures.

outflowing flames/fuel and incoming air. In this case, more oxygen is entrained and reacted with fuel near the opening and is thereby more sensitive to the pressures. In contrast, the 0.272 opening factor exhibits minimal sensitivity to pressure change, attributable to its extremely limited ventilation, which is near the lower bound of chamber HRR, rendering variations in chamber HRR versus pressure insignificant.

Figure 8a shows façade temperature distributions under altitude effect for HRRs of 600–900 kW, with the same opening dimension as in the experiments ($W \times H = 0.9\,\text{m} \times 0.9\,\text{m}$). At each HRR, lower pressure results in larger high-temperature areas. This effect can be attributed to increased HRR outside the chamber, meaning more fuel burns near or outside the opening. With respect to the pressure impact on façade flames, temperature distributions of comparable external HRRs as indicated by the black-dashed line in Figure 8d that is 101.3 kPa to 900 kW and 58.7 kPa to 750 kW (highlighted by red front in figure (a)) are compared. The overall temperature distribution expands with smaller high-temperature zones at lower pressure, due to lower oxygen entrainment mass flow rate caused by reduced air density, which facilitates fuel combustion expansion.

Furthermore, the conditions highlighted by the red dashed circle in Figure 8d illustrate the altitude effect under varied opening shapes by combining Figure 8b,c, which is also marked using different color fonts. In these temperature distributions, a red-dashed line at 540°C indicates visible flames, enabling a quantitative comparison of the altitude effect. The altitude-driven enhancement rates in flame height between 101.3 and 82.5 kPa are 1.1, 1.3, and 1.4 for square, vertical, and horizontal openings, respectively, showing that altitude has the greatest impact—and thus highest fire risk—on horizontal openings. It can be seen that for the same external HRRs, a transition from horizontal to vertical openings results in the flame detaching from the façade, with an increase in flame thickness but a reduction in flame area. This difference in enhancement rates can be attributed to varying air entrainment capacities. In the case of the square opening, flames detach from the façade, allowing air supply from the front, behind, and both sides [31]. With a vertical opening, the flame also detaches, but the entrainment from the front and back is restricted, as the width is nearly half of that in the square opening. For horizontal openings, the flame remains attached to the façade, similar to the front entrainment in the square opening, but with insufficient air supply from behind and both sides due to full attachment to the façade, as shown in Figure 8c. As atmospheric pressure decreases, reducing effective oxygen percentage, the limited air supply shifts combustion to higher positions, leading to an order of fire risk across openings: horizontal > vertical > square.

Figure 9 presents the impacts of HRR, opening shape, and pressure on the temperatures along ejected flame trajectories. Flame temperatures increase with decreasing pressure, and this enhancement is consistent across various HRRs and opening shapes. Cross points emerge as pressure varies, with their heights significantly rising when the opening shape transitions from square to vertical and subsequently to horizontal. The formation of these cross points is attributed to two factors:

1. Decreases in opening factors and pressures result in more fuel combustion outside the chamber, elongating the high-temperature region of flames above the cross point.
2. Lower effective oxygen percentages at reduced pressures limit oxygen mass entrainment rate, restricting combustion near the opening (below the cross point) and reducing ejected flame temperatures.

For horizontal openings (Figure 9c), temperatures near the opening decrease by approximately 100°C as HRRs increase from 600 to 900 kW. This occurs because larger amounts of fuel burned outside the chamber expand the high-temperature flame regions, reducing the availability of entrained air for the inner flame and lowering its trajectory temperatures. Notably, a sudden temperature drop appears at 82.5 kPa in the 750 kW case for horizontal openings, particularly at lower heights above the opening, which is absent in the 600 and 900 kW HRRs. Comparing Figure 9a–c reveals that 750 kW represents a transitional state regarding sufficient air entrainment for the inner flame. For pressures above 82.5 kPa, adequate air entrainment along the flame trajectory is sustained, whereas at pressures below 82.5 kPa, rich fuel combustion along the façade raises flame temperatures. Under 82.5 kPa, limited inner flame air entrainment combined with relatively less fuel combustion yields lower flame temperatures, as visualized in the 750 kW temperature distribution in Figure 8c.

3.4 | Characterization of Flame Temperature Considering Opening and Altitude Variations

In Yokoi's work [3], the temperatures of ejected flames are characterized under the assumption that the neutral plane is located at half the height of the opening. A length scale $r_0 = \sqrt{WH/2\pi}$ is defined, where W and H are the width and height of the opening, respectively, representing the radius of a circle whose area equals half the opening's area, treated as the heat source. Using this length scale, a non-dimensional correlation, Θ versus z/r_0, is proposed to describe the temperature variation along the vertical axis:

$$\Theta = \frac{\Delta T_z r_0^{5/3}}{\sqrt[3]{\frac{Q^2 T_a}{c_p^2 \rho_z^2 g}}} = \text{function}\left(\frac{z}{r_0}\right) \tag{1}$$

Here, z represents the vertical distance from the neutral plane (m), T_a is the ambient temperature (K), ΔT_z denotes the temperature rise above ambient at location z (K), Q is the convective HRR (kW) at the opening, and c_p and ρ_z are specific heat capacity (kJ/(kg/K)) and density (kg/m^3) of ejected gases, respectively. Since the neutral plane is designated at $H/2$, the convective HRR Q is expressed as:

$$Q = C_d c_p \rho_g \Delta T_g W \int_0^{H/2} v \mathrm{d}z \tag{2}$$

Combining with the outflow velocity $v = \sqrt{\frac{2gz\Delta T_g}{T_a}}$, Equation (2) can be integrated becomes:

$$Q = \frac{2}{3}\sqrt{2}\left(\frac{1}{2}\right)^{\frac{2}{3}} C_d c_p \rho_g \Delta T_g W (H)^{\frac{3}{2}} \sqrt{\frac{\Delta T_g g}{T_a}} \tag{3}$$

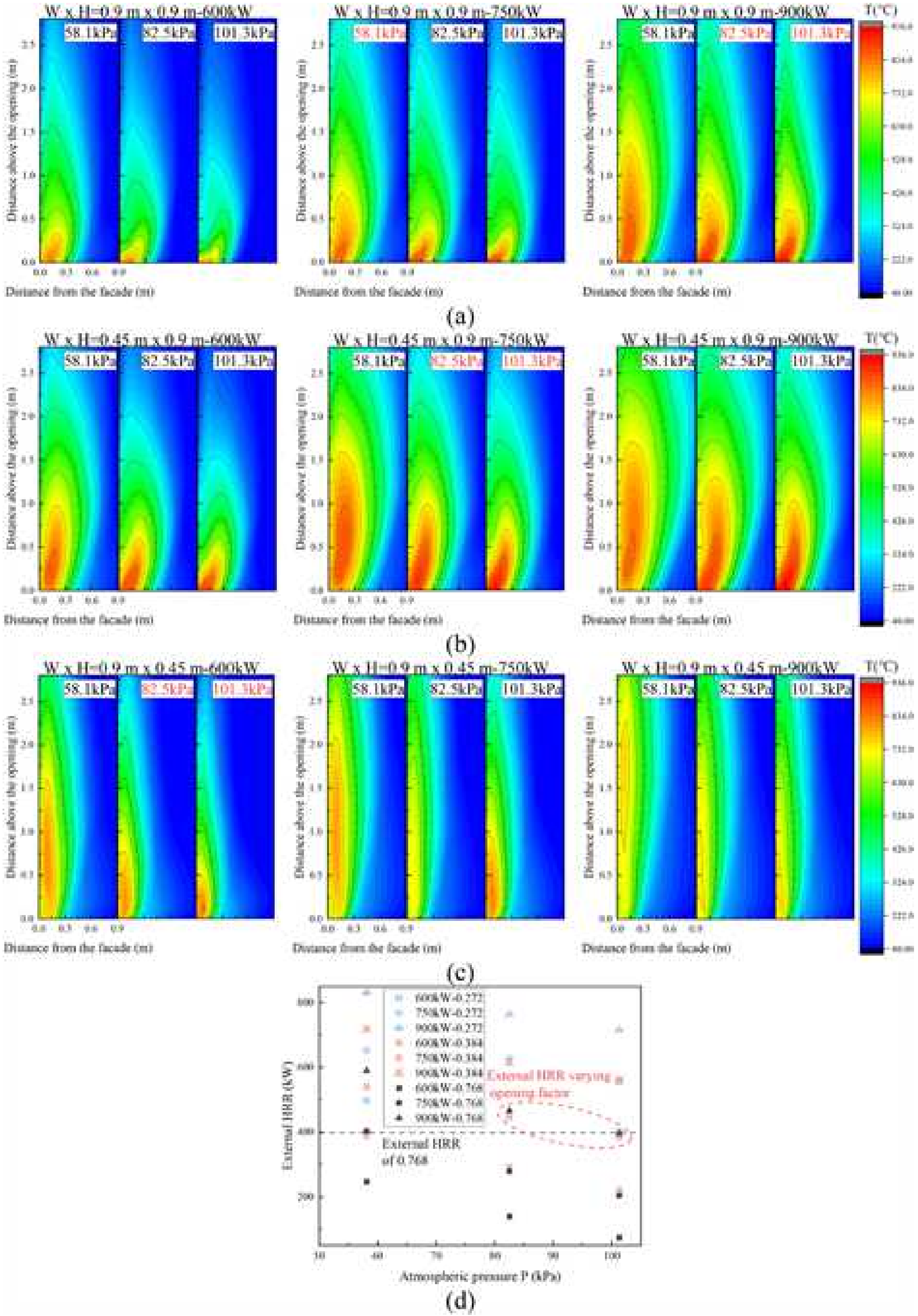

FIGURE 8 | Legend on next page.

FIGURE 8 | Altitude effect on façade temperature distributions of (a) square ($A\sqrt{H}=0.768$), (b) vertical ($A\sqrt{H}=0.384$), and (c) horizontal openings ($A\sqrt{H}=0.272$) under varied HRRs, and (d) corresponding HRR outside the chamber.

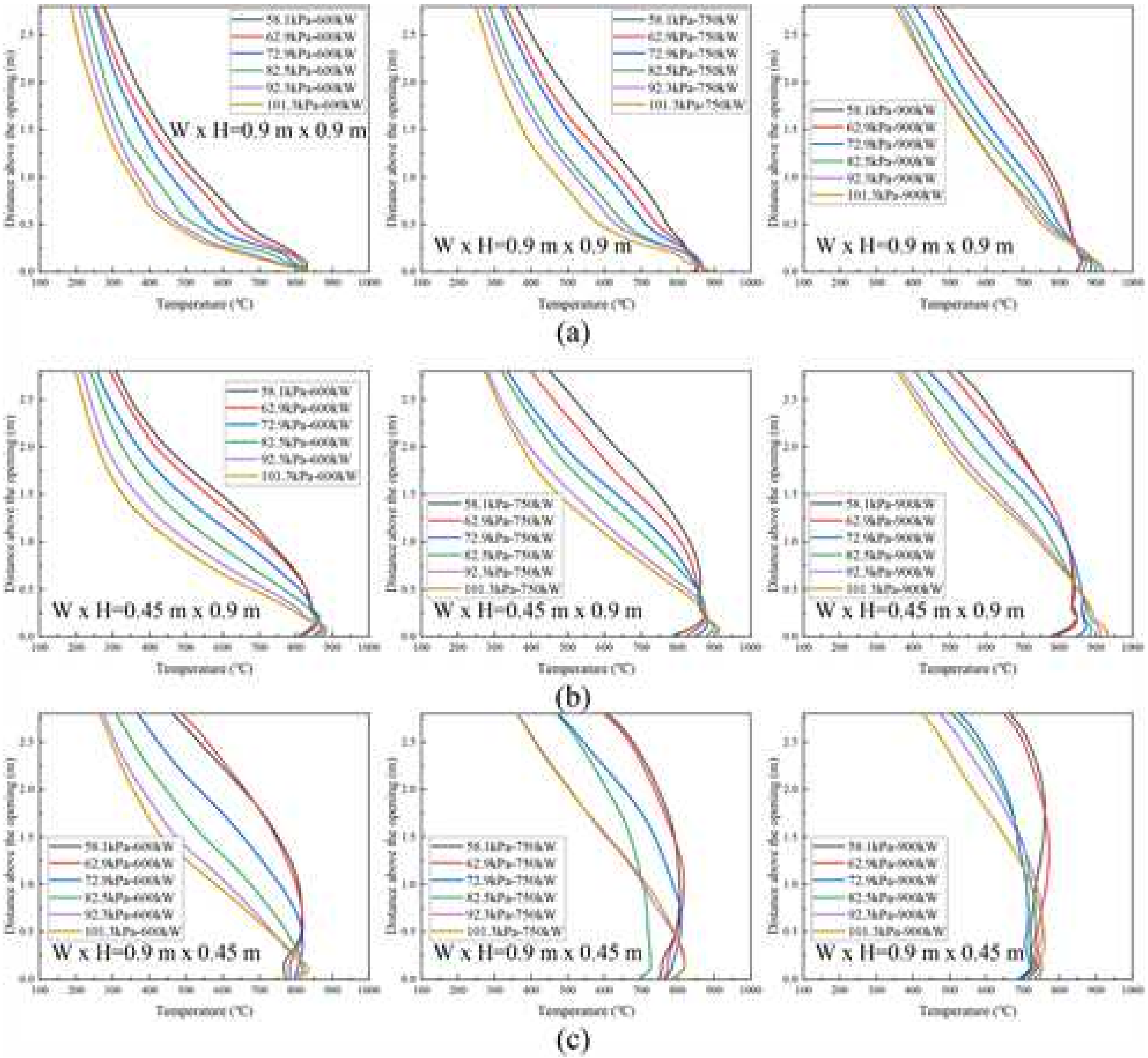

FIGURE 9 | Altitude effect on flame temperatures of (a) square ($A\sqrt{H}=0.768$), (b) vertical ($A\sqrt{H}=0.384$), and (c) horizontal openings ($A\sqrt{H}=0.272$) under varied HRRs.

Rearranging Equation (3), a constant relationship is obtained:

$$\frac{(\Delta T_g)^{\frac{2}{3}}\left[\rho_g/\rho_a W(H)^{\frac{2}{3}}\right]}{Q\sqrt{T_a}/\rho_a c_p\sqrt{g}} = \text{constant} \tag{4}$$

Considering that the Yokoi model demonstrates the dependency of the non-dimensional temperature Θ on varying opening shapes, a revised length scale $\widetilde{l_1}$ is introduced based on the examination of Equation (4) [28]:

$$\widetilde{l_1} = \left(\frac{\rho_g}{\rho_a}W(H)^{3/2}\right)^{2/5} = \left(\frac{\rho_g}{\rho_a}AH^{1/2}\right)^{2/5} \tag{5}$$

In this case, the Yokoi-Lee model is derived as:

$$\widetilde{\Theta} = \frac{\Delta T_z r_0^{5/3}}{\sqrt[3]{\frac{Q^2 T_a}{c_p^2 \rho_a^2 g}}} = \text{function}\left(\frac{z}{\widetilde{l_1}}\right) \tag{6}$$

Compared to the original Yokoi model, the length scale r_0 and hot gas density ρ_g are replaced by $\widetilde{l_1}$ and ambient air density ρ_a, which guarantees the convergence of non-dimensional temperature at the neutral plane.

Based on the modeled flame temperatures, Figure 10 presents the correlation of $\widetilde{\Theta}$ versus $z/\widetilde{l_1}$ across different opening shapes,

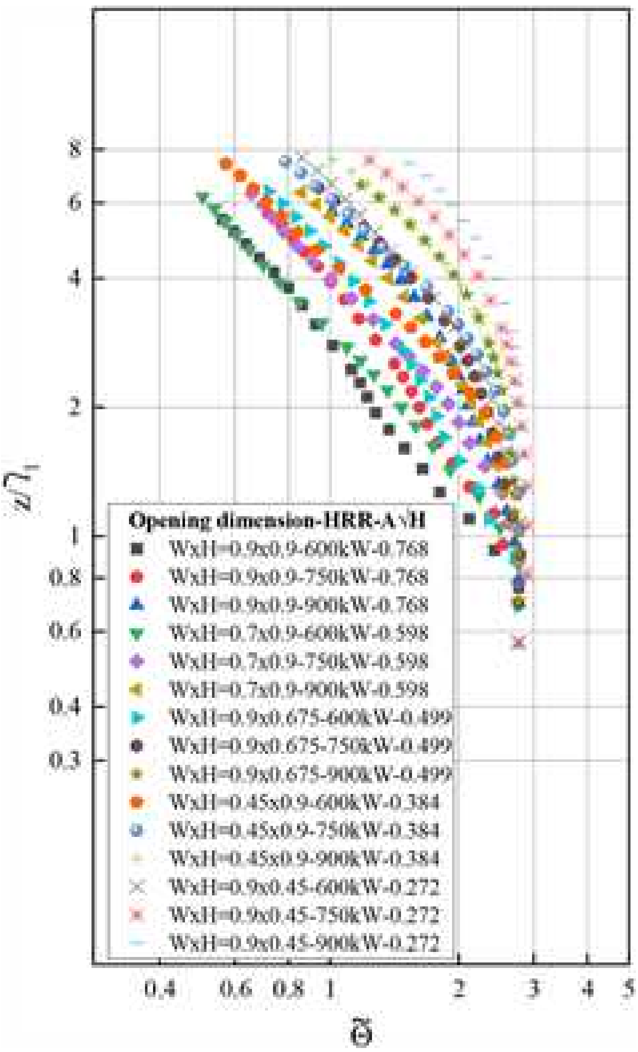

FIGURE 10 | Dimensionless temperature $\widetilde{\Theta}$ versus normalized height $z/\widetilde{l}_1$ of Yokoi-Lee model at 101.3 kPa with varied opening factors and HRRs.

HRRs at the standard pressure. Yokoi's theory, developed from reduced-scale façade flames in well-ventilated conditions [32], derives flame temperatures based on the convective HRR, is limited by not considering the fuel combustion outside the opening as illustrated in Equation (2). However, Figure 10 reveals different HRRs occurring outside the chamber, indicating incomplete fuel combustion within the chamber and additional combustion outside the opening—characteristic of under-ventilated fires. Therefore, the Yokoi-Lee model converges the flame temperature at approximately $\widetilde{\Theta} = 2.76$ for normalized height $z/\widetilde{l}_1 < 1$ but diverged significantly with increasing HRRs and decreasing opening factors. This divergence arises from increased fuel combustion occurring outside the opening, which amplifies flame intensity and elongates high-temperature regions. For instance, as shown in Figure 7, the configuration of $W \times H = 0.9\,\text{m} \times 0.45\,\text{m}$ at 900 kW exhibits the highest external HRR, corresponding in Figure 10 to the most pronounced elongation of the continuous flame region. To address combustion outside the chamber in under-ventilated fires, a non-dimensional external HRR Q^*_{ext} is defined [33]:

$$Q^*_{\text{ext}} = \frac{Q_{\text{ext}}}{\rho_a c_p T_a \sqrt{g} l_1^{5/2}} \qquad (7)$$

Where Q_{ext} is the HRR outside the chamber, and $l_1 = \left(\text{AH}^{1/2}\right)^{2/5}$ represents an appropriate length scale for under-ventilated compartment fires, relating to the convective heat flow. Additionally, considering that the flame temperature rise ΔT_z above a certain heat source is correlated with HRR by a power dependence of 2/5 [34], the specified HRR factor $Q' = 1/\left(Q^*_{\text{ext}}\right)^{2/5}$ is introduced to characterize the variation of the continuous flame region induced by external HRRs and opening factors. The improved Yokoi-Lee model is expressed as:

$$\widetilde{\Theta} = \frac{\Delta T_z r_0^{5/3}}{\sqrt[3]{\frac{Q^2 T_a}{c_p^2 \rho_a^2 g}}} = \text{function}\left(\frac{z \cdot Q'}{\widetilde{l}_1}\right) \qquad (8)$$

The improved Yokoi-Lee model shows the convergence of flame temperatures under varying opening factors, HRRs, and pressures, as depicted in Figure 11. The results show that the characterized flame temperatures show improved convergence across different HRRs and opening factors. Compared to the original Yokoi-Lee model, the range of the continuous flame (the high-temperature region with minimal temperature decreases) in $z/\widetilde{l}_1$ expands from 0.56–1 to 0.4–2, whereas its non-dimensional temperature $\widetilde{\Theta}$ remains relatively stable. In the intermittent flame region ($(z \cdot Q')/\widetilde{l}_1 > 2$), the enlargement or mitigation of $\widetilde{\Theta}$ depends on fuel combustion near the opening, regulated by the introduced HRR factor Q'. However, the performance of convergence is further affected by altitude effect, that is non-dimensional temperatures $\widetilde{\Theta}$ increases for smaller opening factors when pressure decreases.

According to the prior analysis in Section 3.3, atmospheric pressure significantly impacts chamber HRR and the temperature distribution of façade flames due to the limited mass entrainment rate of oxygen. Therefore, understanding how pressure limits air entrainment and the influence of opening factors on altitude effects is crucial for characterizing façade flame temperatures. To normalize this relationship, the non-dimensional chamber HRR $Q_p^* = Q_p/Q_0$ and pressure $P^* = P/P_0$ are defined, where Q_0 and P_0 are the chamber HRR and pressure at the standard altitude, and Q_p and P are those at elevated altitudes. Figure 12a presents the correlation of Q_p^* versus P^*, treated as passing through the origin of the coordinates. Unlike Figure 7, it is evident that the altitude effect is sensitive to opening shapes, with horizontal openings being more affected by pressure variations. Furthermore, Figure 12b presents the correlation between slopes and opening factors, indicating that the altitude effect is amplified as the opening factor decreases.

Combining the correlations determined in Figure 12b, the opening-dependent altitude effect on flame air entrainment is quantified as: $Q_p^* = (-0.78\,AH^{1/2} + 1.37) \cdot (P^* - 1) + 1$. By incorporating Q_p^*, the HRR factor becomes $Q'_p = \left(Q^*_p / Q^*_{\text{ext}}\right)^{2/5}$. Thus,

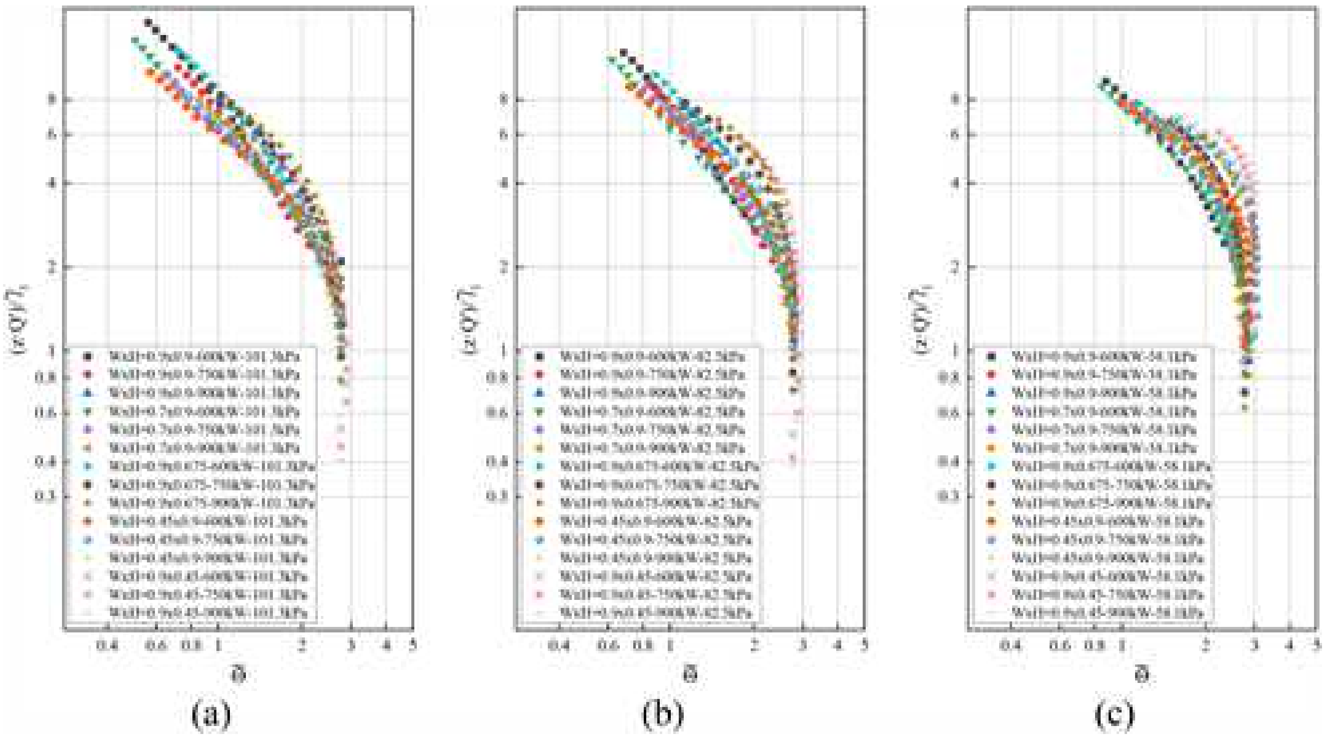

FIGURE 11 | Convergence of improved Yokoi-Lee model with varied opening factors and HRRs at pressures of (a) 101.3 kPa, (b) 82.5 kPa, and (c) 58.1 kPa.

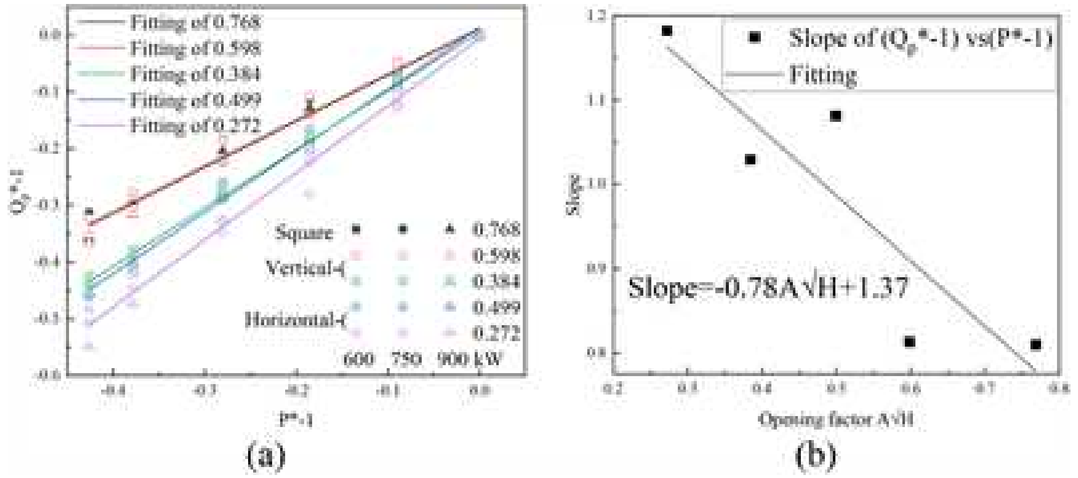

FIGURE 12 | (a) Q_p* varying P* under different opening factors, and (b) corresponding correlation between slopes and opening factors.

the improved Yokoi-Lee model, accounting for the altitude effect, is expressed as:

$$\widetilde{\Theta} = \frac{\Delta T_z r_0^{5/3}}{\sqrt[3]{\frac{Q^2 T_a}{c_p^2 \rho_a^2 g}}} = \text{function}\left(\frac{z \cdot Q'_p}{\widetilde{l_1}}\right) \tag{9}$$

The convergence of the improved Yokoi-Lee model, accounting for altitude effects, is presented in Figure 13. By introducing the new HRR factor Q'_p, the model achieves convergence not only at the standard atmospheric pressure of 101.3 kPa but also under subatmospheric pressures. The elongation of continuous and intermittent flame regions is mitigated as pressure decreases, with the effect being particularly pronounced for the opening factors under horizontal shapes. According to the comprehensive evaluation in Figure 13b:

1. The continuous flame (Region 1) is consistently regulated for $(z \cdot Q'_p)/\widetilde{l_1} < 2$ with a non-dimensional temperature $\widetilde{\Theta}$ of 2.76.
2. The intermittent flame (Region 2) remains collapsed along a slope of −0.83, showing acceptable convergence across varied opening factors, HRRs, or pressures.

It should be noted that the convergence of the improved Yokoi-Lee model is achieved within the limitations of the current configurations, including HRRs of 600–900 kW, propane as fuel, opening factors of 0.272–0.768, and the designated platform of JIS A 1310. Its further implementation requires evaluation under specific conditions.

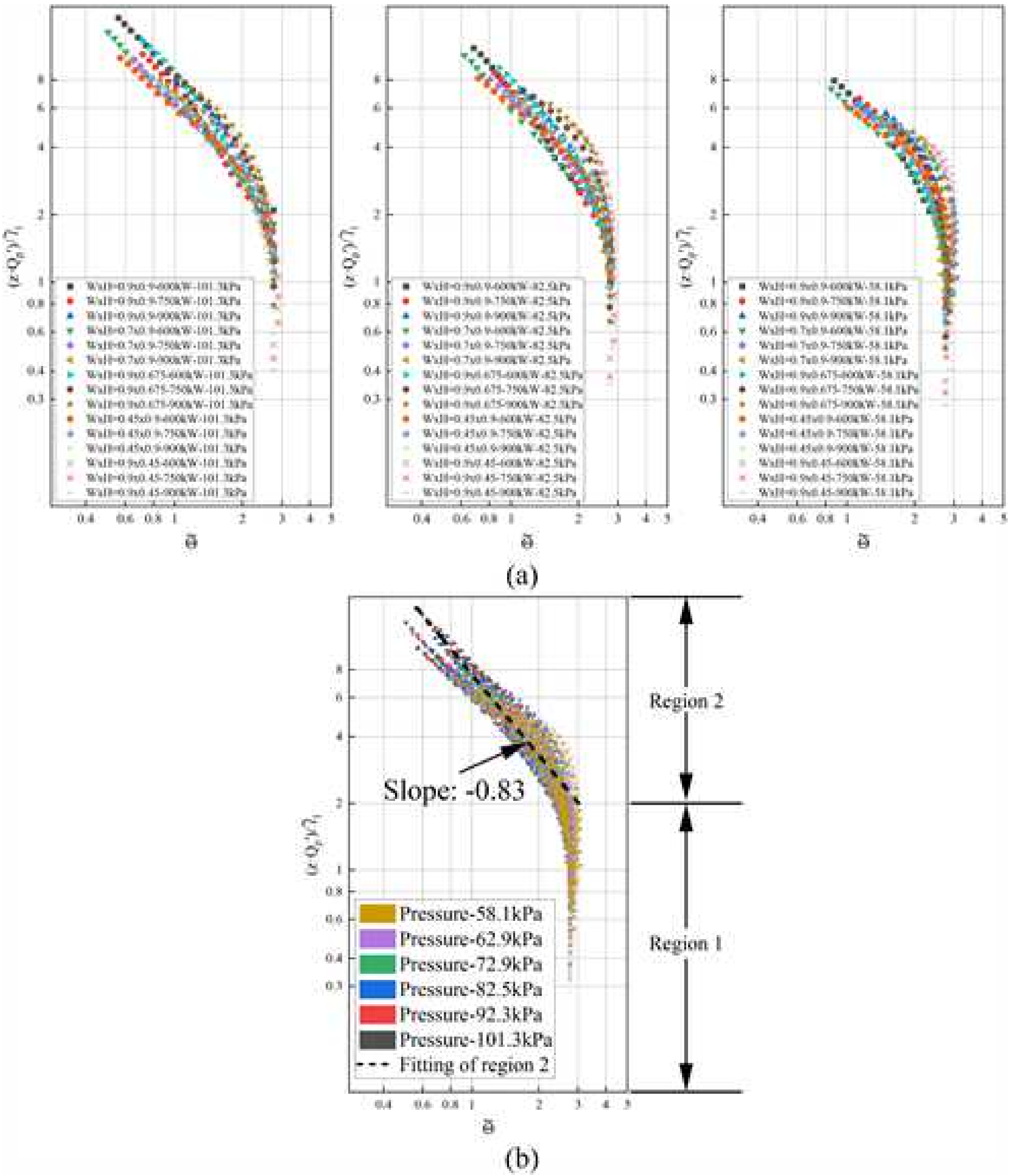

FIGURE 13 | Convergence of improved Yokoi-Lee model accounting for altitude effect at (a) different pressures and (b) comprehensive evaluation.

4 | Conclusion

In this study, the altitude effect on ejected flame during façade calibration tests is investigated over a range of HRRs, opening shapes, and atmospheric pressures. The analysis is conducted based on the combination of JIS A 1310 standard tests and CFD modeling. Major findings include:

1. In the large-scale experiments of JIS A 1310, the trends of vertical temperature distributions at different horizontal distances from the façade indicate that the flame turning point—the transition where flame behavior shifts from horizontal momentum-dominated to buoyancy-dominated—is minimally influenced by variations in input HRRs in the case of apparent ejected flames, which

are affected by the temperature of ejected flames, that is HRR inside the chamber.

2. The flame temperatures of modeling are in good qualitative agreement compared to the experimental measurements. The modeling discrepancies are attributed to the simplifications in soot modeling, which contribute to temperature underestimation in the soot-poor region near the opening but temperature overestimation in the soot-rich region at the higher part of the façade.
3. The façade flames or temperature distribution are expanded at subatmospheric pressure due to lower oxygen entrainment mass flow rate caused by reduced air density, which facilitates fuel combustion volume expansion. Also, the opening shape tends to alter the detachment and reattachment of ejected flames, which further changes the flame air entrainment. In this case, the fire risk under the altitude effect can be ranked as horizontal > vertical > square openings.
4. The improved Yokoi-Lee model is proposed to characterize the flame temperature. By introducing a non-dimensional HRR factor Q_p', the model accounts for the elongation of flame regions caused by fuel combustion outside the opening and achieves acceptable convergence across varying HRRs, opening factors, and atmospheric pressures. However, its convergence is attained within the limitations of the current configurations, including fuel type, HRR range, and geometry. Therefore, its applicability should be further evaluated under specific conditions.

Acknowledgments

The authors would like to gratefully acknowledge the helpful discussions with Drs. Yi Wang, Ning Ren, Xiaoyi Lu, and Gaurav Agarwal from FM Global. This work was supported by the project of JSPS Kakenhi grant number 22KK0062.

Conflicts of Interest

The authors declare no conflicts of interest.

Data Availability Statement

The data that support the findings of this study are available from the corresponding author upon reasonable request.

References

1. K. Al-Kodmany, “Skyscrapers in the Twenty-First Century City: A Global Snapshot,” *Buildings* 8, no. 12 (2018): 175.

2. N. White and M. Delichatsios, *Fire Hazards of Exterior Wall Assemblies Containing Combustible Components* (Springer, 2015).

3. S. Yokoi, “Study on the Prevention of Fire-Spread Caused by Hot Upward Current,” (1960), Eport no. 34. Japan: Building Research Institute.

4. M. Delichatsios, “Enclosure and Façade Fires: Physics and Applications,” *Fire Safety Science* 11 (2014): 3–27.

5. Y. Ohmiya, Y. Hori, K. Safimori, and T. Wakamatsu, “Predictive Method for Properties of Flame Ejected From an Opening Incorporating Excess Fuel,” (2000), Paper presented at: Proceed of 4th Asia-Oceania Symposium on Fire Science and Technology.

6. B. Zhou, H. Yoshioka, T. Noguchi, and T. Ando, “Experimental Study on Vertical Temperature Profile of Buoyant Window Spill Plume From Intermediate-Scale Compartments,” *Fire and Materials* 44, no. 4 (2020): 79–88.

7. “List of Highest Large Cities,” https://en.wikipedia.org/w/index.php?title=List_of_highest_large_cities&oldid=1242562515.

8. G. S. La Paz, “Bolivia Guide: What to See Plus the Best Bars, Restaurants and Hotels,” (2017), https://www.theguardian.com/travel/2017/dec/09/la-paz-bolivia-guide-best-things-to-do-bars-hotels-restaurants#img-1.

9. “Dali City,” https://en.wikipedia.org/w/index.php?title=Dali_City&oldid=1253530012.

10. X. Ma, R. Tu, C. Ding, Y. Zeng, L. Xu, and T. Fang, “Experimental Study on Thermal Safety Analysis of Flexible Polyurethane at Various Facade Inclined Structures Under Low Ambient Pressure Condition,” *Engineering Structures* 176 (2018): 11–19.

11. X. Ma, R. Tu, Y. Zeng, and T. Fang, “An Analysis of Low Ambient Pressure on Fire Risks Associated With Rigid Polyurethane Building Façade Insulation Under Various Width Constructions,” *Indoor and Built Environment* 28, no. 7 (2019): 905–913.

12. X. Ma, R. Tu, X. Cheng, S. Zhu, Q. Sun, and T. Fang, “Sub-Atmospheric Pressure Coupled With Width Effect on Downward Flame Spread Over Energy Conservation Material Polyurethane Foam,” *Journal of Thermal Science* 29 (2020): 115–121.

13. X. Ma, R. Tu, C. Ding, Y. Zeng, Y. Wang, and T. Fang, “Thermal and Fire Risk Analysis of Low Pressure on Building Energy Conservation Material Flexible Polyurethane With Various Inclined Facade Constructions,” *Construction and Building Materials* 167 (2018): 449–456.

14. J. Yin, W. Yao, Q. Liu, et al., “Experimental Study of n-Heptane Pool Fire Behavior in an Altitude Chamber,” *International Journal of Heat and Mass Transfer* 62 (2013): 543–552.

15. F. Wu, R. Zhou, G. Shen, J. Jiang, and K. Li, “Effects of Ambient Pressure on Smoke Back-Layering in Subway Tunnel Fires,” *Tunnelling and Underground Space Technology* 79 (2018): 134–142.

16. J. Ji, F. Guo, Z. Gao, J. Zhu, and J. Sun, “Numerical Investigation on the Effect of Ambient Pressure on Smoke Movement and Temperature Distribution in Tunnel Fires,” *Applied Thermal Engineering* 118 (2017): 663–669.

17. JIS A 1310:2019, “Test Method for Fire Propagation Over Building Facades,” (2019), In. Japan: Published By: Japanese Standards Association (JSA).

18. X. Sun, H. Yoshioka, T. Noguchi, et al., “Large Eddy Simulations Fire Modeling of JIS A 1310 Façade Calibration Test With Respect to Sidewall,” *Fire and Materials* 48, no. 4 (2024): 411–425.

19. Atmosphere US, “US Standard Atmosphere,” (1976), National Oceanic and Atmospheric Administration.

20. “fireFoam-dev,” https://github.com/fireFoam-dev.

21. N. Ren and Y. Wang, “A Convective Heat Transfer Model for LES Fire Modeling,” *Proceedings of the Combustion Institute* 38, no. 3 (2021): 4535–4542.

22. N. Ren, Y. Wang, S. Vilfayeau, and A. Trouvé, “Large Eddy Simulation of Turbulent Vertical Wall Fires Supplied With Gaseous Fuel Through Porous Burners,” *Combustion and Flame* 169 (2016): 194–208.

23. B. Zhou, H. Yoshioka, M. Kanematsu, and T. Noguchi, “Numerical and Experimental Study of Cedar Façade Fire,” *Fire and Materials* 46, no. 2 (2022): 476–486.

24. C. Fureby, G. Tabor, H. Weller, and A. Gosman, “A Comparative Study of Subgrid Scale Models in Homogeneous Isotropic Turbulence,” *Physics of Fluids* 9, no. 5 (1997): 1416–1429.

25. B. F. Magnussen and B. H. Hjertager, “On Mathematical Modeling of Turbulent Combustion With Special Emphasis on Soot Formation and Combustion,” (1977), Paper Presented at: Symposium (international) on Combustion.

26. S. Kim and J. Kim, “Effect of Radiation Model on Simulation of Water Vapor-Hydrogen Premixed Flame Using Flamelet Combustion Model in OpenFOAM,” *Nuclear Engineering and Technology* 54, no. 4 (2022): 1321–1335.

27. Y. Ohmiya, S. Kang, M. Noaki, and M. Delichatsios, “Effects of Opening Aspect Ratio on Facade Gas Temperatures With and Without Sidewalls for Underventilated Conditions,” *Fire Safety Journal* 113 (2020): 102944.

28. Y. P. Lee, M. A. Delichatsios, and Y. Ohmiya, “The Physics of the Outflow From the Opening of an Enclosure Fire and Re-Examination of Yoko's Correlation,” *Fire Safety Journal* 49, no. 15 (2012): 82–88.

29. L. Seigel, “The Projection of Flames From Burning Buildings,” *Fire Technology* 5, no. 1 (1969): 43–51.

30. K. Xu, Y. Wu, H. Shen, Q. Zhang, and H. Zhang, “Predictions of Soot Formation and Its Effect on the Flame Temperature of a Pulverized Coal-Air Turbulent Jet,” *Fuel* 194 (2017): 297–305.

31. K. Himoto, T. Tsuchihashi, Y. Tanaka, and T. Tanaka, “Modeling the Trajectory of Window Flames With Regard to Flow Attachment to the Adjacent Wall,” *Fire Safety Journal* 44, no. 2 (2008): 250.

32. M. A. Delichatsios, G. W. H. Silcock, X. Liu, M. Delichatsios, and Y. P. Lee, “Mass Pyrolysis Rates and Excess Pyrolysate in Fully Developed Enclosure Fires,” *Fire Safety Journal* 39, no. 1 (2004): 1–21.

33. Y. P. Lee, M. A. Delichatsios, and G. W. H. Silcock, “Heat Fluxes and Flame Heights in Facades From Fires in Enclosures of Varying Geometry,” *Proceedings of the Combustion Institute* 31, no. 2 (2007): 2521–2528.

34. C. Gong, L. Ding, H. Wan, J. Ji, Z. Gao, and L. Yu, “Spatial Temperature Distribution of Rectangular n-Heptane Pool Fires With Different Aspect Ratios and Heat Fluxes Received by Adjacent Horizontal Targets,” *Fire Safety Journal* 112 (2020): 102959.